Eur. Phys. J. C (2024) 84:251
https://doi.org/10.1140/epjc/s10052-024-12601-3

THE EUROPEAN PHYSICAL JOURNAL C

Regular Article - Experimental Physics

Radiation hardness of MALTA2 monolithic CMOS imaging sensors on Czochralski substrates

Milou van Rijnbach[1,2,a], **Dumitru Vlad Berlea**[3], **Valerio Dao**[1], **Martin Gaži**[4], **Phil Allport**[5], **Ignacio Asensi Tortajada**[1], **Prafulla Behera**[6], **Daniela Bortoletto**[4], **Craig Buttar**[7], **Florian Dachs**[1], **Ganapati Dash**[6], **Dominik Dobrijević**[1,8], **Lucian Fasselt**[3], **Leyre Flores Sanz de Acedo**[1], **Andrea Gabrielli**[1], **Laura Gonella**[5], **Vicente González**[9], **Giuliano Gustavino**[1], **Pranati Jana**[6], **Long Li**[5], **Heinz Pernegger**[1], **Francesco Piro**[1], **Petra Riedler**[1], **Heidi Sandaker**[2], **Carlos Solans Sánchez**[1], **Walter Snoeys**[1], **Tomislav Suligoj**[8], **Marcos Vázquez Núñez**[1,9], **Anusree Vijay**[6], **Julian Weick**[1,10], **Steven Worm**[3], **Abdelhak M. Zoubir**[10]

[1] CERN, Geneva, Switzerland
[2] University of Oslo, Oslo, Norway
[3] DESY, Zeuthen, Germany
[4] University of Oxford, Oxford, UK
[5] University of Birmingham, Birmingham, UK
[6] Indian Institute of Technology Madras, Chennai, India
[7] University of Glasgow, Glasgow, UK
[8] University of Zagreb, Zagreb, Croatia
[9] Universitat de València, Valencia, Spain
[10] Technische Universität Darmstadt, Darmstadt, Germany

Received: 8 September 2023 / Accepted: 22 February 2024

Abstract MALTA2 is the latest full-scale prototype of the MALTA family of Depleted Monolithic Active Pixel Sensors (DMAPS) produced in Tower Semiconductor 180 nm CMOS sensor imaging technology. In order to comply with the requirements of high energy physics (HEP) experiments, various process modifications and front-end changes have been implemented to achieve low power consumption, reduce random telegraph signal (RTS) noise, and optimise the charge collection geometry. Compared to its predecessors, MALTA2 targets the use of a high-resistivity, thick Czochralski (Cz) substrates in order to demonstrate radiation hardness in terms of detection efficiency and timing resolution up to 3×10^{15} 1 MeV n_{eq}/cm^2 with backside metallisation to achieve good propagation of the bias voltage. This manuscript shows the results that were obtained with non-irradiated and irradiated MALTA2 samples on Cz substrates from the CERN SPS test beam campaign from 2021 to 2023 using the MALTA telescope.

1 History of the MALTA family

Monolithic CMOS pixel sensors provide several advantages over hybrid pixel sensors for high energy physics (HEP) experiments. These include the possibility for large area production, lower costs, and reduced production effort and material usage. Additionally, monolithic sensor designs featuring a small collection electrode can be operated with low noise due to the reduced sensor capacitance. These sensors are expected to play a crucial role in future particle physics experiments and have been the focus of various R&D projects over the past decade [1]. They are now approaching a mature stage of development as they are being implemented in several HEP experiments, such as ALICE [2].

MALTA [3] was developed for potential use in the ATLAS experiment at the High Luminosity LHC (HL-LHC) upgrade and possible integration in other future high-energy physics experiments. Its design targets radiation hardness for fluences $> 10^{15}$ 1 MeV n_{eq}/cm^2 (NIEL) and 1 MGy (TID), thin CMOS sensors with high granularity, high hit-rate capability (> 100 MHz/cm^2), and fast response time (40 MHz). The MALTA matrix is made up of 512×512 pixels at a pitch of 36.4 μm. The small octagonal collection electrode (2 μm diameter) features a small pixel capacitance,

[a] e-mail: milou.van.rijnbach@cern.ch (corresponding author)

Published online: 10 March 2024

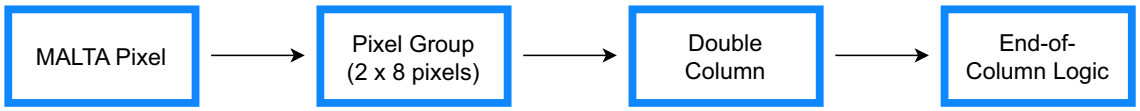

Fig. 1 Schematic flow diagram of the MALTA readout from MALTA pixel to pixel group (comprised of 2×8 pixels) to a double column. Eventually the asynchronous readout sends the hit information to the end-of-column logic via a 22-bit wide bus

offering low noise and low analog power dissipation (70 mW/cm^2). The digital power consumption is 10 mW/cm^2 at 100 MHz/cm^2. Figure 1 shows the MALTA readout flow diagram. The asynchronous readout sends hit information directly from the pixel to the periphery through 37 parallel output signals with a 2 ns output signal length. This avoids distributing high-frequency clock signals across the matrix, minimising analog-digital cross-talk and power consumption. Pixels are organised into 2 × 8 pixel groups. A pixel hit within a group triggers the generation of a reference pulse, which is transmitted on a 22 bit parallel bus to the matrix periphery together with the pixel and group address of the hit pixel. The readout uses two parallel buses, one for even groups and the other for odd groups. The implementation of these two buses reduces cross-talk on the hit address bus as adjacent groups cannot share the same bus [4]. MALTA features a binary readout with no time-over-threshold (ToT) information.

The MALTA sensor is fabricated in a tower semiconductor 180 nm CMOS sensor imaging technology featuring three different pixel flavours, illustrated in Fig. 2. The standard modified process (STD) introduces a low dose n$^-$ layer across the full pixel matrix on top of the p-type substrate. The second process modification includes a design with a gap in the n$^-$ layer (NGAP), and the third pixel design features an additional deep p-well implant (XDPW) [5]. The doping level of the low dose n$^-$ layer is higher than that of the substrate, but relatively low compared to other implants in the process. The NGAP and XDPW pixel flavours have demonstrated to be particularly effective as radiation hard sensors, as they have shown improved detection efficiency in the pixel corners [6]. These pixel flavours are produced for MALTA on high-resistivity p-type epitaxial substrates and high-resistivity p-type Czochralski (Cz) substrates, where the measured resistivity for both substrate types lies between 3 and 4 kΩcm. The results presented in Ref. [4] have shown that MALTA Cz sensors can generate a larger depletion volume, leading to a significantly amplified ionization charge signal in comparison to MALTA sensors on epitaxial substrates. Furthermore, promising results were shown in terms of better radiation hardness and larger cluster size for MALTA Cz sensors compared to the sensors fabricated on epitaxial substrates.

This paper presents the results that were achieved with the next generation MALTA chip, MALTA2, on Cz wafers. The paper will discuss the design modifications that were implemented, with respect to its predecessor, and their implications on the performance. This will be followed by a discussion on the importance of a good backside contact for the Cz wafers. The test beam set-up for sample characterisation will be discussed, including a summary of the various MALTA2 samples used in this study. Finally, test beam results at the super proton synchrotron (SPS) at CERN will be presented on the radiation hardness of MALTA2 Cz samples.

2 MALTA2

MALTA2 is the second full-scale prototype of the MALTA family. The main objectives include expanding the radiation hardness of the design towards higher fluences [6], achieving an uniform in-pixel charge collection efficiency and lowering the random telegraph signal (RTS) noise in the sensor front-end [7]. MALTA2 is approximately half the size of the MALTA sensor, with a matrix of 224 × 512 pixels (9 × 18 mm^2). It inherits the asynchronous readout of the previous generation, but implements modifications in both the slow control and front-end. These modifications underwent validation through a small-scale demonstrator, referred to as mini-MALTA [6].

2.1 Slow control and front-end modifications

The slow control of the original MALTA utilised an Ethernet-like protocol, whereas the mini-MALTA detector, and subsequently in MALTA2, an improved design was realised by incorporating a shift register [8]. This shift register-based slow control not only enabled more efficient configuration of the chip but also demonstrated successful operation in other silicon-based DMAPS technologies [9], thereby facilitating a more reliable implementation. Several changes in the pixel front-end were implemented in order to achieve the aforementioned goals of the MALTA2 variant. As extensively discussed in Ref. [7], an open-loop amplification stage was implemented which allowed for a compact front-end design with lower noise and higher speed of the circuit, suitable for a small collection electrode pixel layout. Multiple cascode transistors were implemented to enhance, among other reasons, the overall gain of the front-end. Large gate areas were implemented for the input and amplification

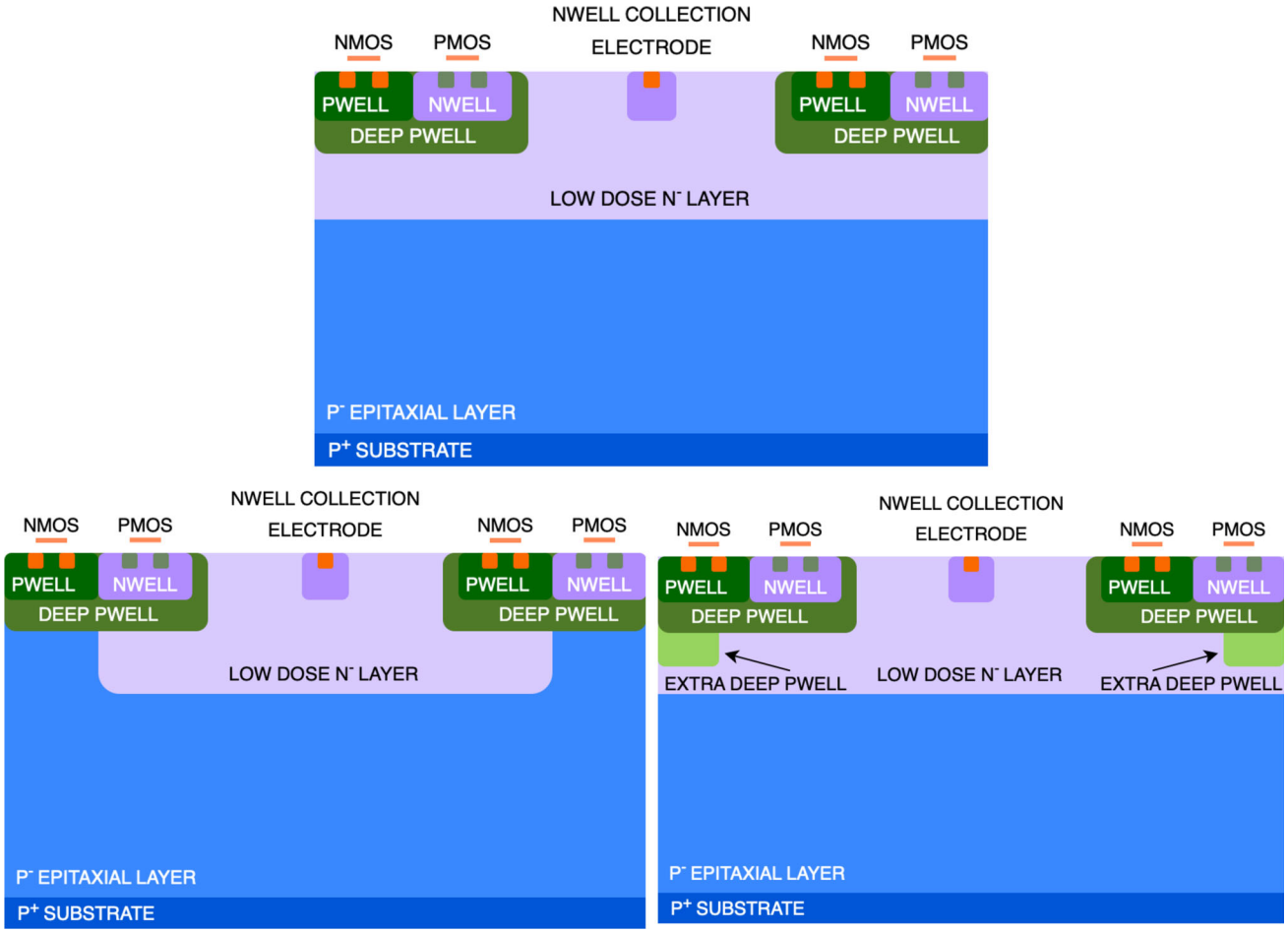

Fig. 2 Cross sections of the process modifications of the Tower Semiconductor 180 nm CMOS imaging technology. Top image shows the standard modified process (STD) where an n^- layer is introduced on top of the p-type substrate. Bottom left image shows the process modification where a gap in the low dose n^- layer is introduced (NGAP). The bottom right image shows the process modification with an extra deep p-well located under the deep p-well (XDPW). Images are not drawn to scale and are adapted from Ref. [5]

stage transistor in order to limit the RTS [7]. The design of the MALTA2 front-end brings improvements in terms of lower noise and the elimination of RTS, demonstrated in Ref. [10].

2.2 Process modifications for radiation hard monolithic CMOS sensors

As highlighted in Ref. [6], on the testing of the mini-MALTA demonstrator, the addition of a lightly-doped (compared to the doping concentration of the collection electrode) n^- layer across the whole area of the pixel is efficient at extending the depletion region in the lateral direction. It allows for the electron–hole pairs that are generated in the active depth, inside the sensing volume, to move through drift. This feature holds higher importance for sensors that are expected to be irradiated to large fluences. In the process of displacement damage, an incident particle or photon can dislodge a silicon atom from its lattice site and hereby create deep level acceptor and donor traps. Trapping sites have a larger impact on charges that travel only via diffusion to the collection electrode. For the MALTA2 sensors, the doping concentration of the deep n^- layer has been modified to gauge its impact on the performance and radiation hardness of the sensor.

Figure 3 highlights the threshold and noise distributions for non-irradiated MALTA2 samples with different doping level of the n^- layer. The naming convention, i.e. high and very high, refers to their relative difference in implantation dose, approximately 70%, and does not refer to the absolute doping concentration itself. At similar threshold, within the expected 10% sample-to-sample variation, a larger noise is observed for the MALTA2 sample with the very high doping of the n^- layer. A comparatively higher doping concentration of the n^- layer reduces the depletion region around the collection electrode, resulting in an effectively larger capacitance and leading to higher noise. This was observed in dedicated TCAD simulations in Ref. [11]. However due to

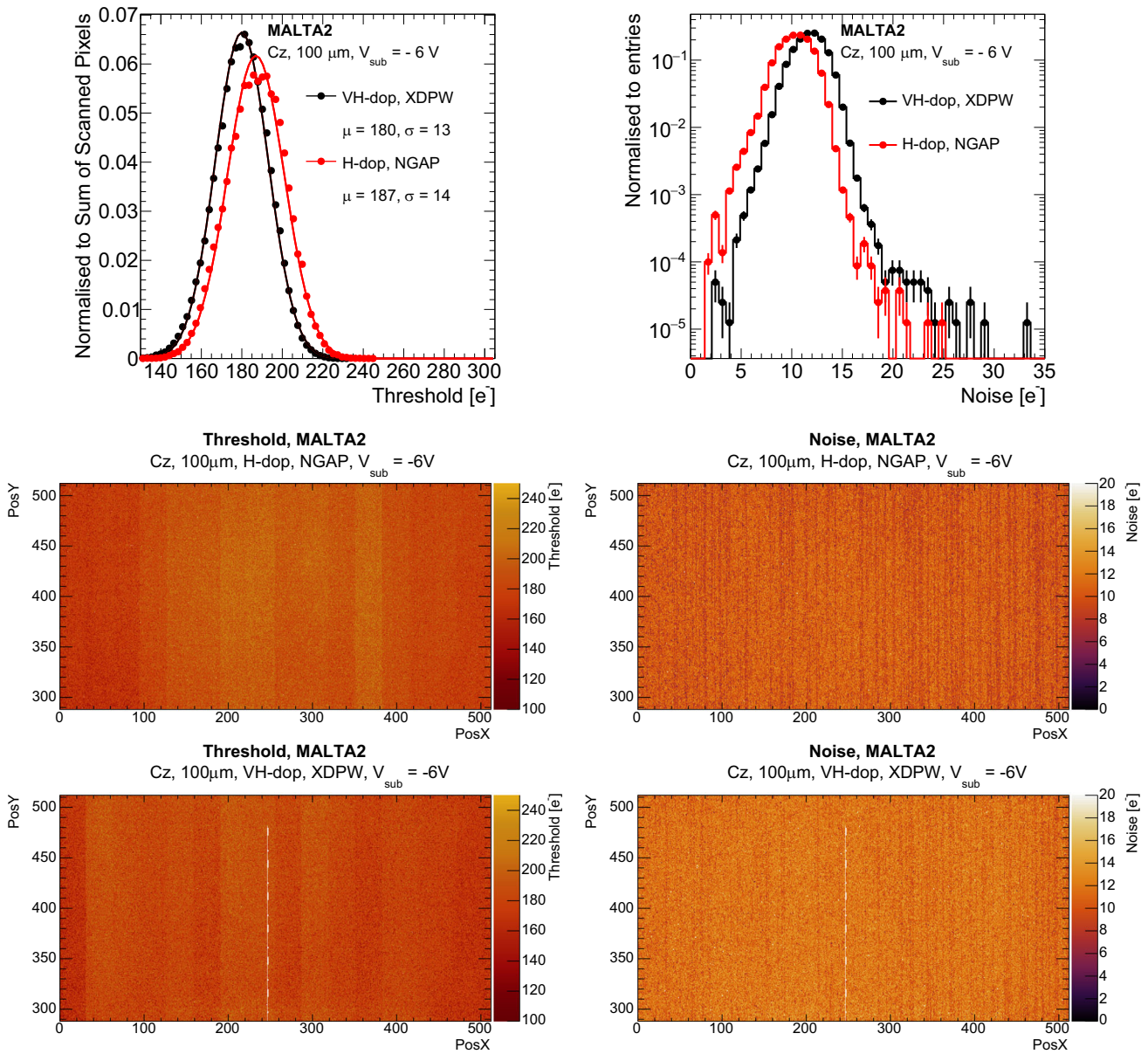

Fig. 3 Threshold distribution (top left image) and noise distribution (top right image), of non-irradiated MALTA2 (Cz, 100 µm) NGAP, high doping of n^- layer (in red) and XDPW, very high doping (in black) at $V_{sub} = -6$ V. Threshold corresponds to ∼180 e^-. The cut-off for the noise distribution at 2 e^- is correlated to the granularity of the noise scan. Additionally the corresponding 2D distribution for the entire matrix of the high doping sample are shown (middle images) and for the very high doping sample (bottom images)

the aforementioned 10% sample-to-sample variation, larger statistics are required to correlate these observations. The 2D threshold maps of Fig. 3 show that the threshold is uniformly distributed in the column (Y) direction, whereas a small variation in threshold along the row (X) direction of the matrix is observed, which is correlated to the front-end biasing scheme. Power pads are distributed on the left and right side of the matrix, leading to an incremental horizontal power voltage drop [7]. Additionally, the noise is distributed uniformly across the entire matrix. A very small noise tail indicates that there is only a minor contribution from RTS to the total noise.

2.3 Backside processing

Samples produced on a Cz substrate require additional considerations to ensure effective backside voltage propagation, particularly for irradiated samples. Under standard conditions (for non-irradiated samples), voltage propagation from the printed circuit board (PCB) to the chip occurs through the

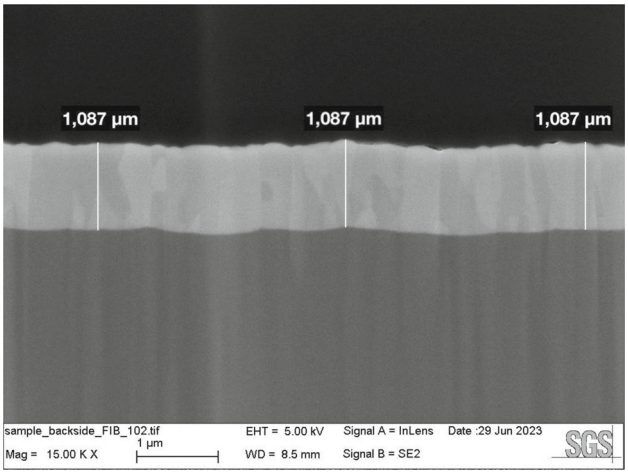

Fig. 4 Cross-sectional SEM image of a MALTA2 sample with backside metallisation. The light grey area indicates the 1 µm thick Aluminium layer

left and right sides of the matrix via an electrically conductive film, Staystik® 571 ($\rho \leq 5 \times 10^{-4}$ Ωcm) [12]. This film is applied along the borders of the hole in the PCB, where the contact with the chip is made. For irradiated Cz samples, an alternative approach involving backside metallisation was explored to ensure uniform bias voltage propagation across the entire chip, especially at elevated bias voltages. The backside metallisation process is carried out by ion beam services (IBS) and comprises four consecutive steps: thinning, implantation, annealing, and aluminum deposition. Initially, the Cz wafer is thinned down using a TAIKO thinning process [13]. This plasma etching step is carefully executed to achieve the desired substrate thickness while preserving the mechanical stability of the wafers throughout the process. Subsequently, boron is used as the dopant for the p-type implantation step. After implantation, the samples are placed in a Rapid Thermal Anneal (RTA) chamber, positioned on a silicon support that facilitates temperature measurement via a pyrometer. In the final step, a 1 µm thick aluminum layer with a tolerance of ± 10% is deposited on the backside of the sample. Figure 4 showcases a scanning electron microscope (SEM) image illustrating a cross-section of a MALTA2 sample with backside metallisation.

3 Test beam set-up for sample characterisation

Between 2021 and 2023, a dedicated test beam campaign was conducted at the super proton synchrotron (SPS) facility of CERN with a 180 GeV hadron beam, using the MALTA telescope [14] to characterise the samples. The main objective of this campaign was to demonstrate the radiation hardness of MALTA2 Cz samples.

3.1 Test beam with the MALTA telescope

The MALTA telescope, a custom pixel telescope, comprises of six MALTA tracking planes (consisting of four epitaxial samples and two Cz samples) and a scintillator for timing reference located behind the telescope planes. It allows to test two devices under test (DUTs) simultaneously and it features a custom cold-box to host irradiated samples in a dry environment at cold temperatures. The trigger system of the telescope is fully configurable, enabling triggering on coincidence between the telescope planes and the scintillator. More information regarding the architecture and performance of the MALTA telescope is available in Ref. [14]. For the alignment, track reconstruction, and offline analysis of the test beam data, the software package Proteus is used [15]. The observables that are used to characterise the DUT, i.e. hit detection efficiency, cluster size and timing resolution, are defined in the sections where the respective results are discussed.

3.2 Sample collection and operating conditions

The MALTA2 sensor has been fabricated with various process modifications. In order to facilitate the understanding of the results presented in Sects. 4 and 5, the various design and operational parameters are explained in more detail below. Due to the limited number of available samples and the wide range of operating parameters, only a subset of these parameters have been individually studied. An overview of the MALTA2 samples studied in this work is provided in Table 1.

Measurements for non-irradiated samples are performed at room temperature, i.e. 20 °C, and measurements with irradiated samples at −20°C. More information on the temperature dependence of the punch-through current and leakage current of irradiated MALTA Cz sensors can be found in Ref. [4]. The samples presented in this study were thinned down to 300 or 100 µm to minimise the material budget. Additionally, all irradiated samples analyzed in this study underwent the backside metallisation (back-metal) process.

Operating threshold

The following sections present results achieved at the operational threshold point where maximum efficiency was attained, while ensuring a noise level per pixel below 40 Hz and a leakage current under 2 mA. The threshold values quoted in this study are derived using capacitance values from injection circuit simulations.

Process modifications

In the context of the MALTA2 Cz samples examined in this study, there are two available flavours: NGAP and XDPW. As demonstrated in Ref. [4], the performance of these two flavours is found to be similar after irradiation. Therefore, the subsequent sections will not discuss the differences in per-

Table 1 Overview of the main specifications of the MALTA2 samples studied in this work. For every sample the fluence level, sensor flavour, and thickness have been indicated. The doping level of the n^- layer is indicated as H (high) and VH (very high). All irradiated samples and one non-irradiated sample underwent backside metallisation (back-metal) during post-processing

Overview of MALTA2 samples							
Fluence [1 MeV n_{eq}/cm^2]	0	0	0	1×10^{15}	2×10^{15}	3×10^{15}	3×10^{15}
Sensor flavour	NGAP	XDPW	XDPW	XDPW	XDPW	XDPW	XDPW
Total thickness [μm]	300	100	100	100	100	100	100
Doping level of n^- layer	H	VH	H	H	H	H	VH
Backside post-processing	None	None	Back-metal	Back-metal	Back-metal	Back-metal	Back-metal

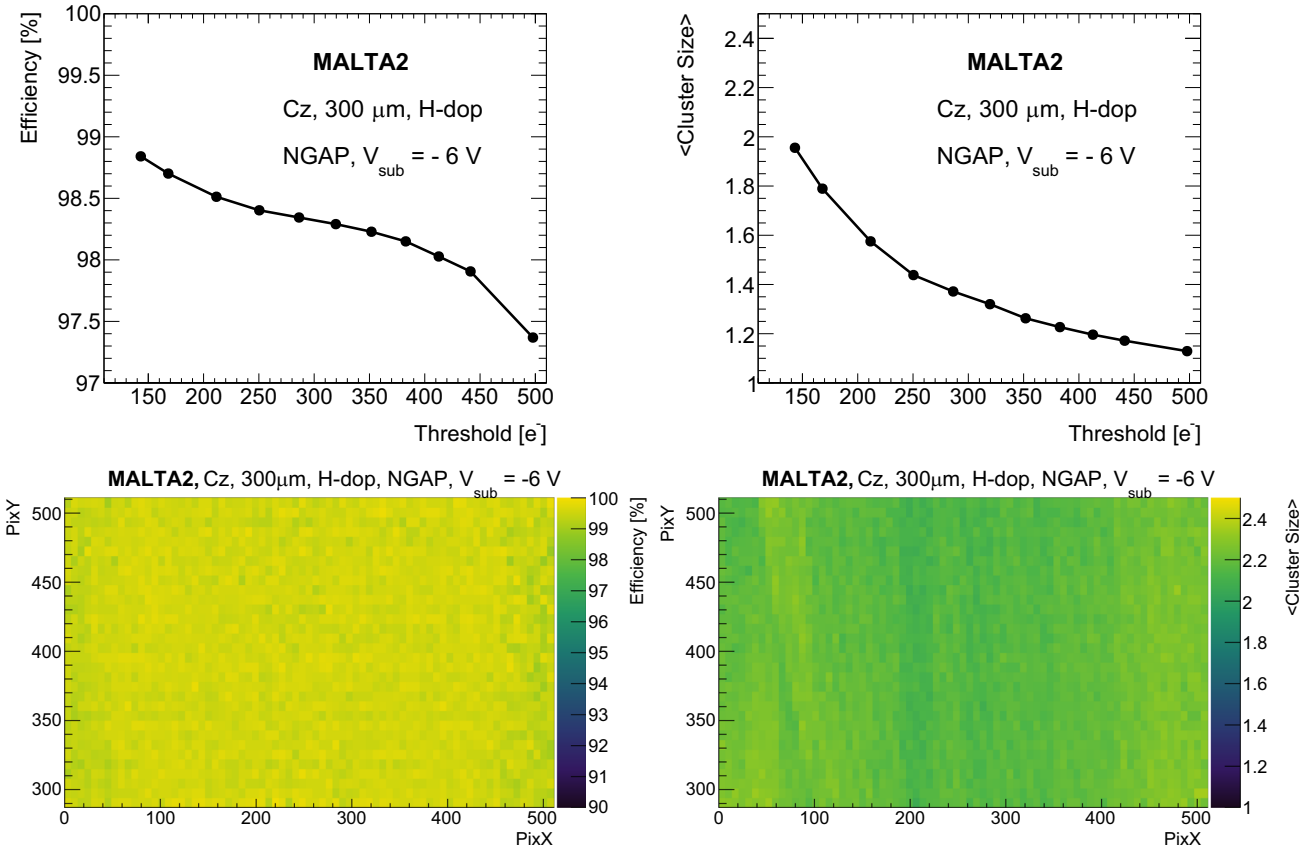

Fig. 5 Average efficiency (top left) and cluster size (top right) as a function of threshold. The bottom images show their respective 2D map at a threshold corresponding to 150 e^-. Results are shown for a non-irradiated MALTA2 sample (Cz, NGAP, 300 μm thick, high doping of n^- layer) at V_{sub}= −6 V

formance between these flavours. Two distinct doping concentrations are present for the continuous n^- layer, denoted as high (H-dop) and very high (VH-dop) doping.

Fluence levels

Results for samples both before and after neutron irradiation are presented. Neutron irradiation was carried out on sensors at the Triga reactor in the Institute Jožef Stefan, Ljubljana, Slovenia, with fluences of 1, 2, and 3 × 10^{15} 1 MeV n_{eq}/cm^2. As a consequence of the irradiation process, the samples experienced a temperature increase to approximately 40 °C [16,17]. Following irradiation, the samples were stored at −20 °C. The duration of irradiation varied based on the chosen fluence, approximately 10 min for a fluence of 1 × 10^{15} 1 MeV n_{eq}/cm^2. The samples have not been subject to any intentional long-term reverse annealing at elevated temperatures.

Bias voltage

The voltage of the p-well and the reset voltage for the collection electrode are fixed at −6 and 0.8 V, respectively. In order to generate a larger drift field in samples with the thick Cz substrate, the reverse bias to the substrate (V_{sub}) is increased. The operational limit of the bias voltage is

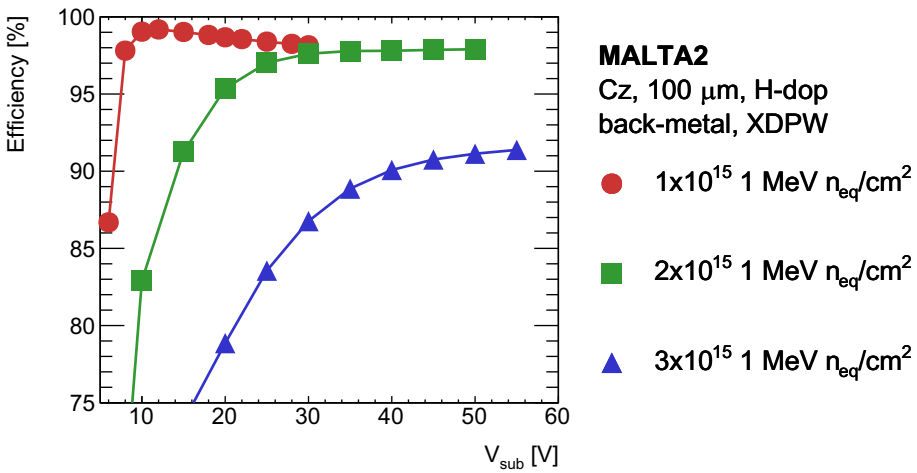

Fig. 6 Average efficiency versus bias voltage for three MALTA2 samples (XDPW, high doping n^- layer, 100 µm thick, and backside metallisation). The samples are irradiated to 1, 2, and 3×10^{15} 1 MeV n_{eq}/cm^2 and the threshold corresponds to 240, 260, and 120 e^-, respectively

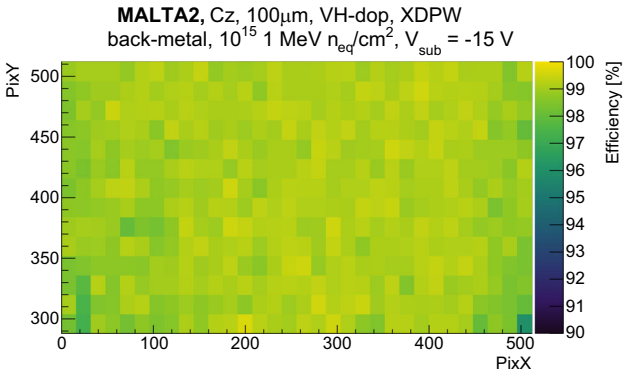

Fig. 7 2D Efficiency map of the entire matrix of a MALTA2 sample (Cz, XDPW, 100 µm thick, high doping of n^- layer and backside metallisation) irradiated to 1×10^{15} 1 MeV n_{eq}/cm^2 and operated at $V_{sub} = -15$ V. The average efficiency is 99% and the threshold corresponds to 240 e^-

restricted by the compliance level (2 mA) in order to protect the electronics. This in turn implies that as the samples have different design variables, i.e. thickness or fluence, the maximum operational substrate bias voltage is sample dependent. For all the results presented in the following sections, the (reverse) substrate bias voltage is specified.

4 Efficiency and cluster size

The hit detection efficiency is calculated as the number of matched clusters on the DUT over the total number of reconstructed tracks. A matched cluster is found by associating hit clusters on the DUT to a track, which should be found within 80 µm from the cluster position. The cluster position is calculated by assigning equal weights to all neighbouring pixel that registered a hit. Due to the very large statistics on the collected events, a small statistical error is recorded for both the hit efficiency and cluster size measurements. During data acquisition, several noisy pixels are masked and their contribution to the total efficiency is taken into account. When full efficiency is obtained, the cluster size becomes a relevant figure of merit as it allows to improve the spatial resolution as demonstrated in the MALTA telescope application [14].

4.1 Before displacement damage

Non-irradiated MALTA2 samples have been characterised in terms of efficiency and cluster size performance for multiple threshold configurations at the default substrate voltage setting of $V_{sub} = -6$ V. Figure 5 highlights the increase in these figures of merit with a decrease in threshold, due to the enhanced detection of hits with low signal amplitude, such as charge sharing between pixels and hits in the pixel corners. With operational threshold settings below $\sim 250\,e^-$, the detection of a larger number of shared charge events yields a large increase in cluster size and a relatively smaller increase in efficiency. Additionally, both an uniform efficiency and cluster size response are observed across the entire pixel matrix. A similar trend in efficiency and cluster size versus threshold was observed between samples with high and very high doping of the n^- layer. The noise per pixel for non-irradiated samples was found to be negligible ($< 1 \times 10^{-3}$ Hz).

4.2 After displacement damage

Figure 6 illustrates the increase in average efficiency with substrate voltage for three MALTA2 samples irradiated at different fluences while operated at a similar threshold value. All samples feature the same doping concentration of the n^- layer (high). For the 1×10^{15} 1 MeV n_{eq}/cm^2 sample, a large efficiency is achieved (99%) at relatively low substrate voltage ($V_{sub} = -10$ V). With elevated radiation damage (2×10^{15} 1 MeV n_{eq}/cm^2), a higher substrate voltage is required to obtain high efficiency. For the 3×10^{15} 1 MeV n_{eq}/cm^2 sample, only an efficiency of 90% is recovered. The increase in punch-through voltage with increasing fluence level was

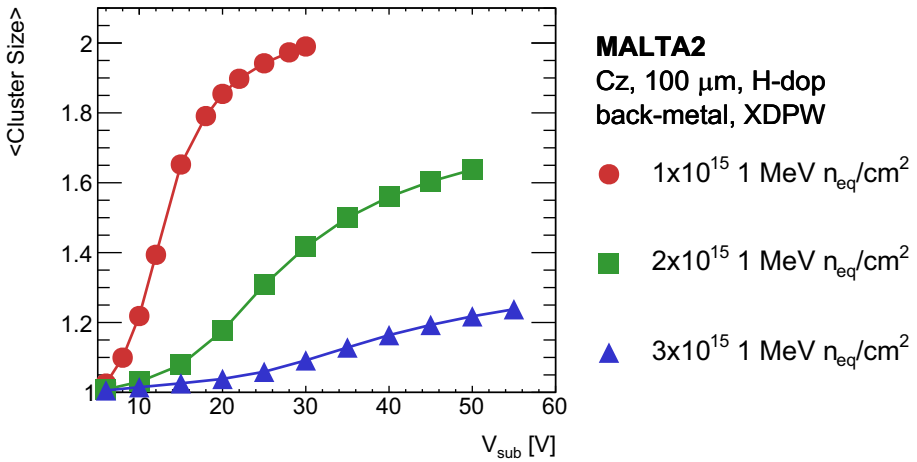

Fig. 8 Average cluster size versus bias voltage for three MALTA2 samples (XDPW, high doping n^- layer, 100 µm thick, and backside metallisation). The samples are irradiated to 1, 2, and 3×10^{15} 1 MeV n_{eq}/cm^2 and the threshold corresponds to 240, 260, and 120 e^-, respectively

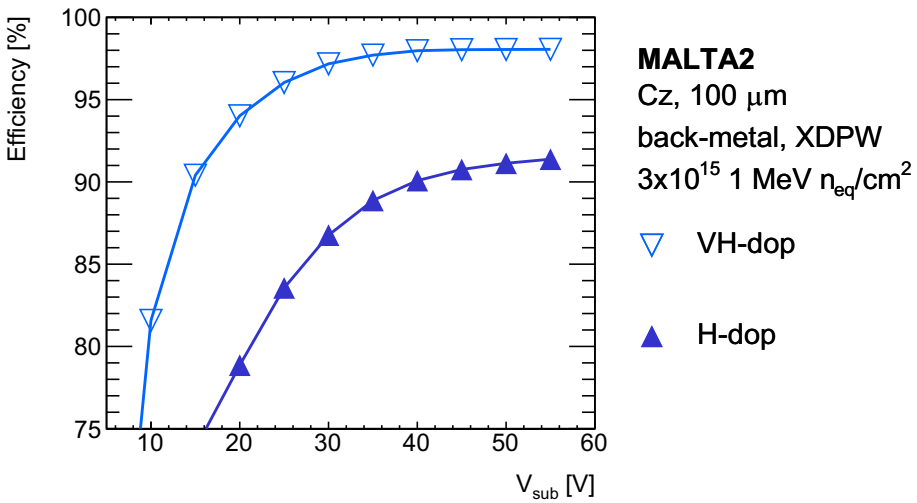

Fig. 9 Average efficiency versus bias voltage for two MALTA2 samples (Cz, XDPW, 100 µm thick, and backside metallisation) irradiated to 3×10^{15} 1 MeV n_{eq}/cm^2. The samples differ in the doping level of the n^- layer, i.e. high and very high, and the threshold corresponds to 120 and 110 e^-, respectively

similarly observed in Ref. [4] on the MALTA Cz sensor. The possible explanation for this behaviour was attributed to the so-called double junction model [18], where irradiation causes the creation of deep-level donors, which adds effective n-doping near the p-well. This further increases the potential barrier between p-well and p-type substrate. In relation to the leakage current, no observations were recorded outside the operational limits (i.e. leakage current under 2 mA and noise level per pixel below 40 Hz). Furthermore, Fig. 7 demonstrates that for a MALTA2 sample irradiated to 1×10^{15} 1 MeV n_{eq}/cm^2, the efficiency is uniformly distributed across the entire matrix.

Figure 8 illustrates the relation between the average cluster size and substrate voltage for the same samples presented in Fig. 6. The average cluster size increases with elevated substrate voltages, due to the enhanced charge sharing effect between pixels for larger active depths in the Cz substrate. With elevated fluence, a large cluster size is recovered by increasing the substrate voltage. The impact of the substrate voltage on the average cluster size for the various fluence levels is similar to the efficiency response, with a large average cluster size (> 1.8) reconstructed at relatively low substrate voltage ($V_{sub} = -20$ V) for the sample irradiated to 1×10^{15} 1 MeV n_{eq}/cm^2. Lower cluster sizes are found at higher substrate voltages for the samples irradiated to 2 and 3×10^{15} 1 MeV n_{eq}/cm^2. This is attributed to the reduced charge collection of these irradiated samples for several substrate bias points, i.e. where no full efficiency is obtained.

4.3 Effect of the doping level of the n^- layer

A possible explanation for the lower efficiency observed for the sample irradiated to 3×10^{15} 1 MeV n_{eq}/cm^2 in Fig. 6 could be attributed to the doping level of the n^- layer. In order to verify this, a MALTA2 sample with very high doping of the n^- layer has been irradiated to the same fluence level. Figure 9 shows the impact of the doping concentration on the efficiency versus substrate bias voltage for two samples irradiated to 3×10^{15} 1 MeV n_{eq}/cm^2. As shown, the sample with the very high doping of the n^- layer achieves a much higher efficiency ($> 97\%$) at a lower substrate voltage. With radiation damage, the lateral depletion of the n^- layer diminishes. The results suggest that this effect is less pronounced in the sample with a very high doping of the n^- layer. Additionally, these observations suggest that as the (deep) p-well and p-type substrate are not sufficiently separated by the n^-

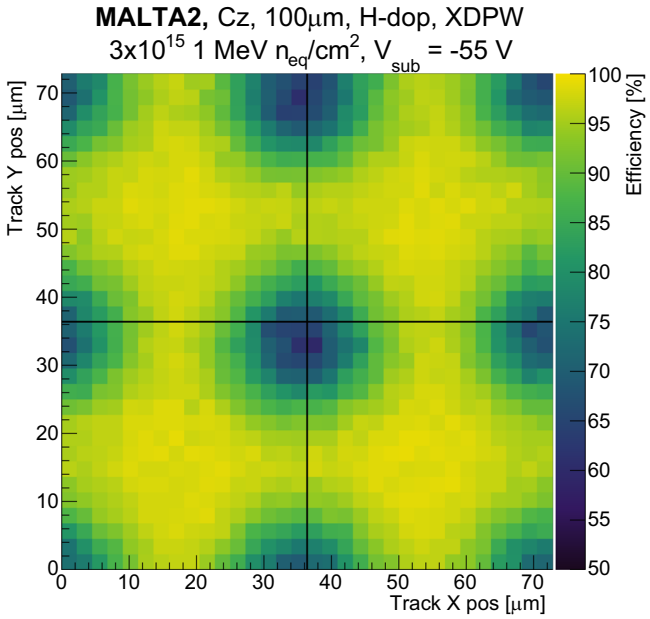

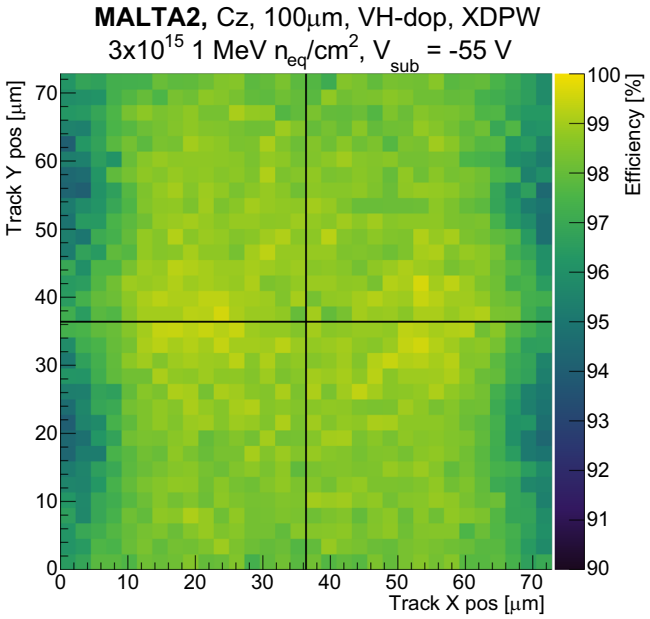

Fig. 10 In-pixel efficiency projected over a 2 × 2 pixel matrix for two MALTA2 samples (Cz, XDPW, 100 µm thick, and backside metallisation) irradiated to 3×10^{15} 1 MeV n_{eq}/cm^2 and operated at $V_{sub} = -55$ V. The samples differ in the doping level of the n^- layer, i.e. high (left) and very high (right), and the threshold corresponds to 120 and 110 e^-, respectively. Note the difference in Z-axis scale

layer, a complete depletion may not be achieved for samples irradiated to high fluences.

Figure 10 shows the in-pixel efficiency after 3×10^{15} 1 MeV n_{eq}/cm^2 irradiation for two samples with different doping concentrations of the n^- layer: high and very high. The efficiency loss for the sample featuring the high doping of the n^- layer originates from the pixel corners, where the diminished electric field degrades the charge collection efficiency. An improvement is observed for the sample with very high doping of the n^- layer, due to the preservation of the initial (non-irradiated) pixel electrical field configuration at high fluences. The loss of efficiency at the edge of the pixel is not a feature of the pixel itself, but rather stems from the data merging of consecutive double columns in the MALTA2 readout.

4.4 Operational window after displacement damage

In order to define an operational window in terms of high efficiency and low noise, the threshold of the in-pixel discriminator and the substrate voltage were systematically varied. The decrease in threshold is expected to increase the number of hit clusters matched to tracks, especially for low charge events such as hits in the pixel corners, at the cost of increasing the detected noise. The increase in substrate voltage increases the effective active depth of the sensor, leading to higher efficiency and elevated noise. As increasing irradiation fluence results in a drop in the measured efficiency and creation

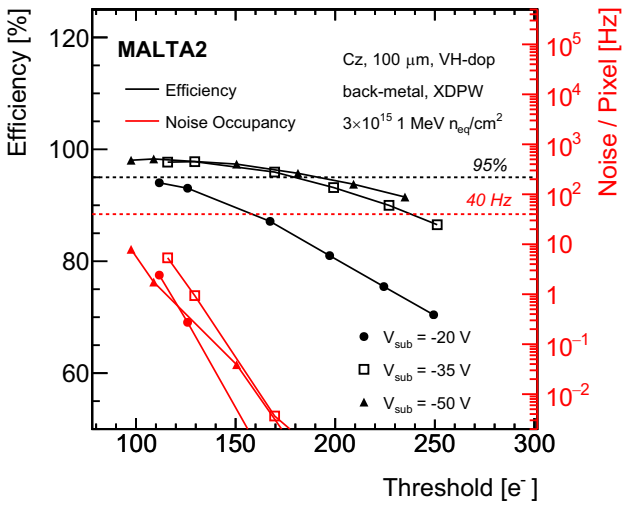

Fig. 11 Average efficiency (in black) and noise occupancy (in red) as a function of threshold in electrons of a MALTA2 sample (Cz, XDPW, very high doping n^- layer, 100 µm, and backside metallisation) irradiated to 3×10^{15} 1 MeV n_{eq}/cm^2. The substrate voltage is set at $V_{sub} = -20, -35, -50$ V. The number of masked pixels is below about 0.02% of the entire chip

of generation-recombination centres that increase the leakage current of the sensor, the sensor noise is enhanced. An operating window for an efficiency > 95% (black lines) and noise per pixel lower than 40 Hz (red lines) for an irradiated sample at 3×10^{15} 1 MeV n_{eq}/cm^2 is found for multiple chip configurations (changing biasing voltage) in Fig. 11. Despite

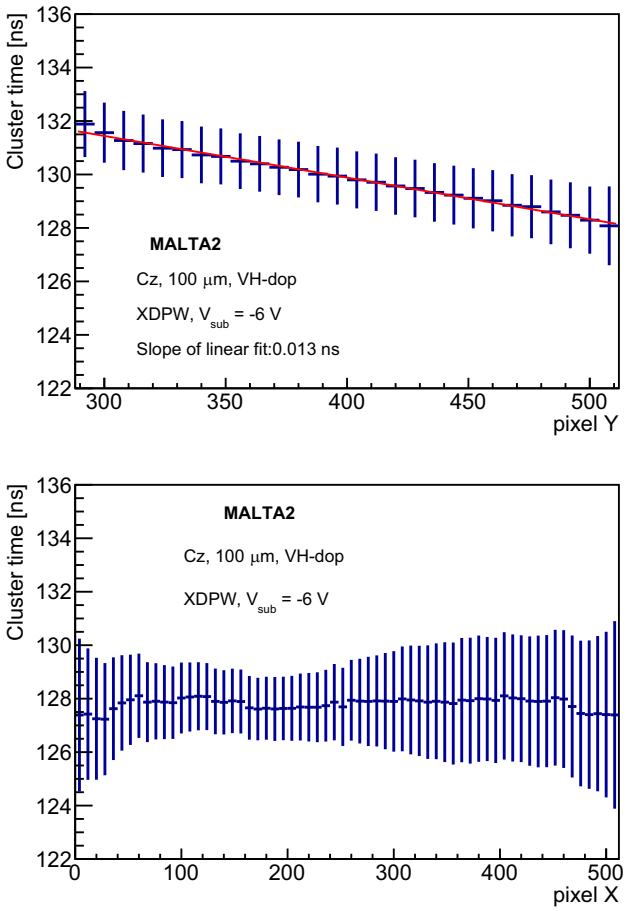

Fig. 12 Time of arrival of the leading hit in the cluster with respect to a scintillator reference along the column (top image) and row direction (bottom image) of the pixel matrix. A correction in the Y-direction is applied due to the time propagation across the column which exhibits a linear behaviour. A correction in the X-direction is applied due to the non-uniformities in the chip response. Error bars represent the corresponding RMS. Both measurements are performed on a MALTA2 sample (Cz, XDPW, very high doping n^- layer, 100 μm thick) at $V_{sub} = -6$ V. The threshold corresponds to 170 e^-

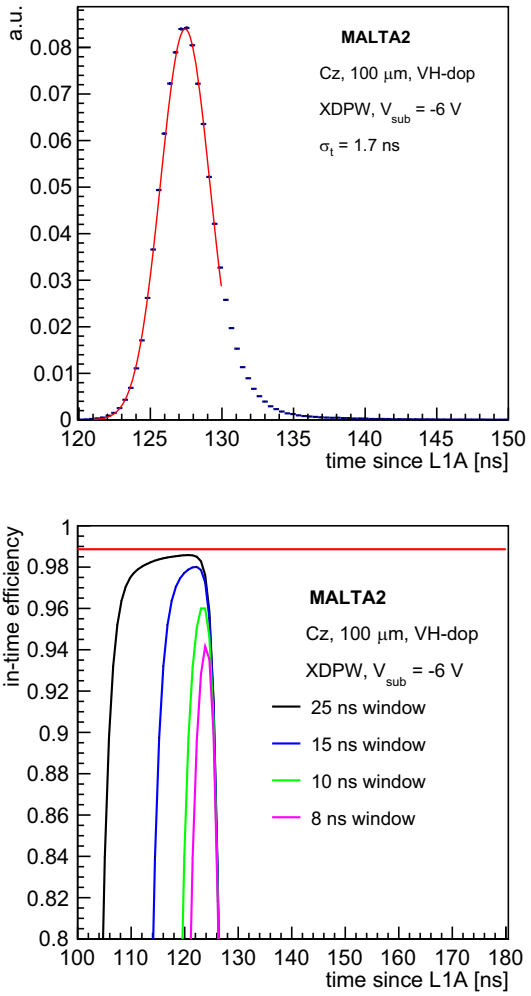

Fig. 13 Top image shows time of arrival of the leading hit in the cluster with respect to a scintillator reference. The quoted $\sigma_t = 1.7$ ns corresponds to the Gaussian fit to the core of the distribution. Bottom image shows in-time efficiency. Black curve corresponds to in-time efficiency within a 25 ns window, blue curve corresponds to a 15 ns windows, and the green and magenta cure represent a 10 and 8 ns window, respectively. Red line represents maximum achievable efficiency without timing constraints. Both measurements are performed on a MALTA2 sample (Cz, XDPW, very high doping n^- layer, 100 μm thick) at $V_{sub} = -6$ V. The threshold corresponds to 170 e^-

the fact that an operating threshold below 200 e^- at substrate bias $V_{sub} < -35$ V is required to achieve >95% efficiency, the low threshold chip configurations still exhibit acceptable noise levels below 40 Hz. The operating window was chosen to comply with the ATLAS ITk requirements [19].

5 Timing performance

The timing characterisation of the MALTA2 sensor front-end has been reported in Ref. [7]. Despite the fact that no ToT is directly available from the chip, the time-walk of the front-end was measured in Ref. [7] using analog output monitoring pixels in the matrix. The time-walk of the front-end was measured to be less than 25 ns for 90% of signals from a ^{90}Sr source. The charged particles generated by the source create minimum ionizing particles (MIP) like signals with a most probable charge deposition of approximately 1800 e^-. However, signals with a time-walk larger than 25 ns were observed for signals with charge depositions below 200 e^-. The time jitter of the front-end electronics was evaluated by charge injection within a pixel using circuitry within the matrix digital readout. The arrival time of hits from the injected charge is compared to the timing of the charge injection trigger pulse transmitted to the chip, by using the PicoTDC with 3 ps binning [20]. The time jitter of the MALTA2 front-end electronics was measured to be 0.17

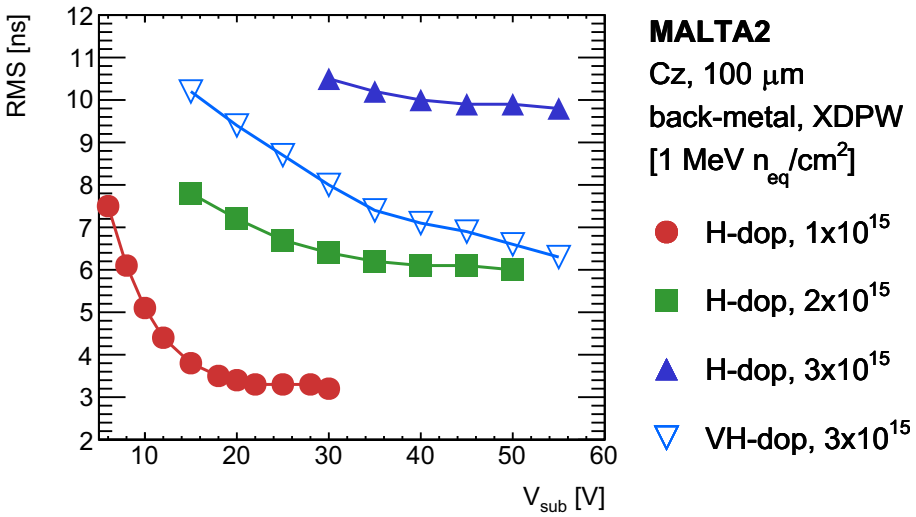

Fig. 14 RMS of timing difference distribution versus bias voltage. Only data points where the detection efficiency lies above 85% are taken into account. Shown here are four MALTA2 samples (XDPW, 100 µm thick, and backside metallisation). Three samples feature the high doping of the n^- layer. They are irradiated to 1, 2, and 3×10^{15} 1 MeV n_{eq}/cm^2 and the threshold corresponds to 240, 260, and 120 e^-, respectively. One sample features the very high doping of the n^- layer. It is irradiated to 3×10^{15} 1 MeV n_{eq}/cm^2 and the threshold corresponds to 110 e^-

ns for charge injection above 1400 e^-, increasing to 4.7 ns at the nominal 100 e^- threshold.

In order to characterise the timing performance of a MALTA2 sample, various intrinsic effects need to be accounted for. As discussed in Ref. [21], the time required to reach the periphery along the column direction in the pixel matrix needs to be corrected for. The signal propagation consists of a contribution of the signal generation inside the pixel group and a contribution from the hit propagation along the matrix column direction to the periphery over an asynchronous parallel bus. As shown in the top image of Fig. 12, this effect exhibits a linear behavior. The error bars represent the corresponding root mean square (RMS). The red line represents the linear fit (with slope of 0.013 ns per pixel), which is in turn used as the correcting function on the timing information in the column (Y) direction. Furthermore, a correction is applied across the row (X) direction of the matrix, shown in the bottom image of Fig. 12. The variation along the X direction is attributed to non-uniformities in the chip response.

5.1 Before displacement damage

The overall MALTA2 timing performance can be assessed by correcting for the aforementioned intrinsic effects and including existing external effects. The timing performance has been measured during the test beam campaigns for both non-irradiated and irradiated chips where a scintillator is used for timing reference. The time delay since the scintillator reference signal is referred to as L1A. The top image of Fig. 13 shows the time of arrival of the fastest hit in a pixel cluster with respect to the scintillator reference. The performance is tested on a Cz MALTA2 chip at $V_{sub} = -6$ V at a threshold value corresponding to 170 e^-. The timing resolution equates to $\sigma_t = 1.7$ ns and is obtained by fitting a Gaussian to the core of the time difference distribution. The distribution contains a jitter contribution from the scintillator ($\sigma_{scintillator} \sim 0.5$ ns) and from oversampling within the FPGA ($\sigma_{FPGA} = 3.125/\sqrt{12} = 0.9$ ns). For HEP applications such as the LHC, sensor signals need to be registered within the bunch-crossing clock of 25 ns. The in-time efficiency for samples was determined by integrating the time-of-arrival distributions (with respect to the scintillator reference) with a sliding window algorithm. The results in the bottom image of Fig. 13 show that for non-irradiated MALTA2 Cz, above 98% of the hits are collected within a 25 ns time window (black) and 90% of the hits are collected within 8 ns (magenta), making it suitable for applications at the HL-LHC and other proposed future collider facilities.

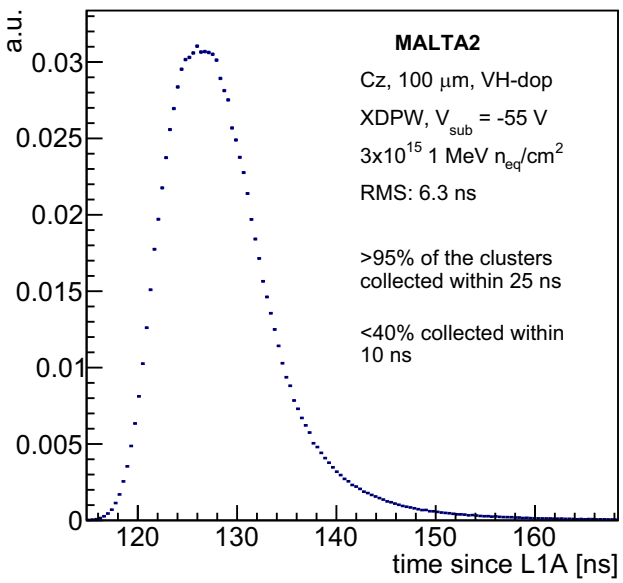

Fig. 15 Time of arrival of leading hit in the cluster with respect to a scintillator reference. Timing measurements are performed on a MALTA2 sample (Cz, XDPW, very high doping of n^- layer, 100 µm thick, and backside metallisation) irradiated to 3×10^{15} 1 MeV n_{eq}/cm^2 and operated at $V_{sub} = -55$ V. Threshold corresponds to 110 e^-

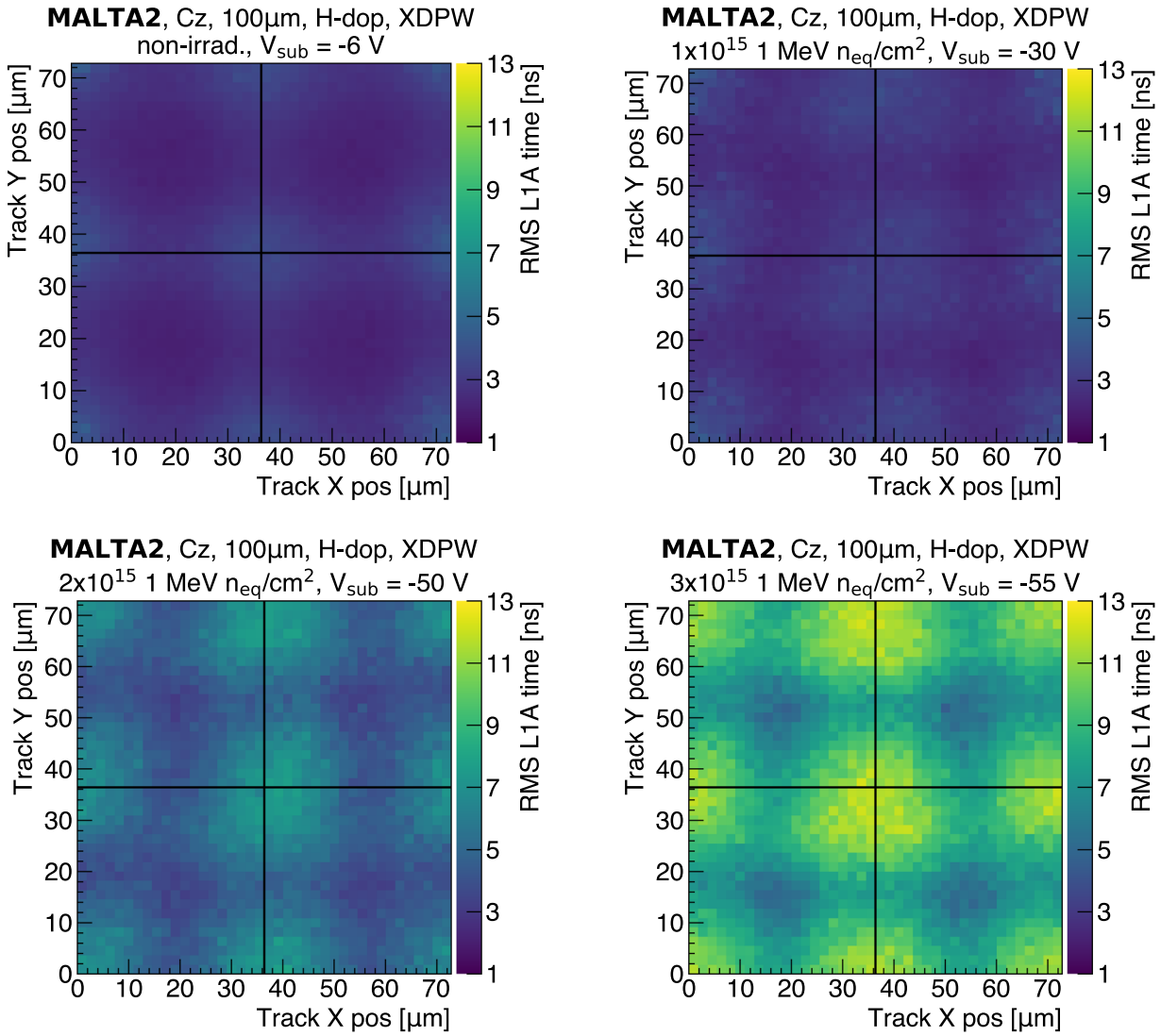

Fig. 16 Projection of the root-mean-squared (RMS) value of the leading hit time within a cluster with respect to a scintillator reference for four MALTA2 samples (Cz, XDPW, high doping of n^- layer, 100 µm thick, and backside metallisation). The samples are irradiated to four different irradiation levels (non-irradiated, 1, 2, and 3×10^{15} 1 MeV n_{eq}/cm^2) and the threshold corresponds to 250, 240, 250, and 120 e^-, at $V_{sub} = -6, -30, -50, -55$V bias voltage, respectively. The leading hit time data are sorted into 1.82×1.82 µm^2 bins based on their associated track position within the pixel extracted from the telescope data. Hits from over the entire chip are projected onto a 2×2 pixel matrix. For each bin, data points which deviate by more than seven RMS from the bin mean value are excluded from the calculation. The operating conditions of the four samples correspond to the data point where the timing RMS is minimised, while the efficiency lies above 90%

5.2 After displacement damage

As mentioned in the previous chapter, the bias voltage of irradiated samples can be increased further, which allows good timing performance to be achieved for samples irradiated at 1, 2, and 3×10^{15} 1 MeV n_{eq}/cm^2. Figure 14 shows the evolution of the RMS of the time difference distribution between the leading hit in the cluster and the scintillator reference as a function of bias voltage for irradiated MALTA2 samples with high and very high doping of the n^- layer. As the timing difference distribution of irradiated samples exhibits a significant tail, a Gaussian fit is not employed, and instead, the RMS is extracted directly from the distribution. Only the cases where the detection efficiency lies higher than 85% are considered (shown in Fig. 6). The results show that for all samples the RMS decreases as the bias voltage is increased. As the substrate voltage and the depleted area increase, a sharper signal pulse is generated due to a greater amount of charge collected. This faster signal with higher amplitude allows for narrower time-difference distributions. The tim-

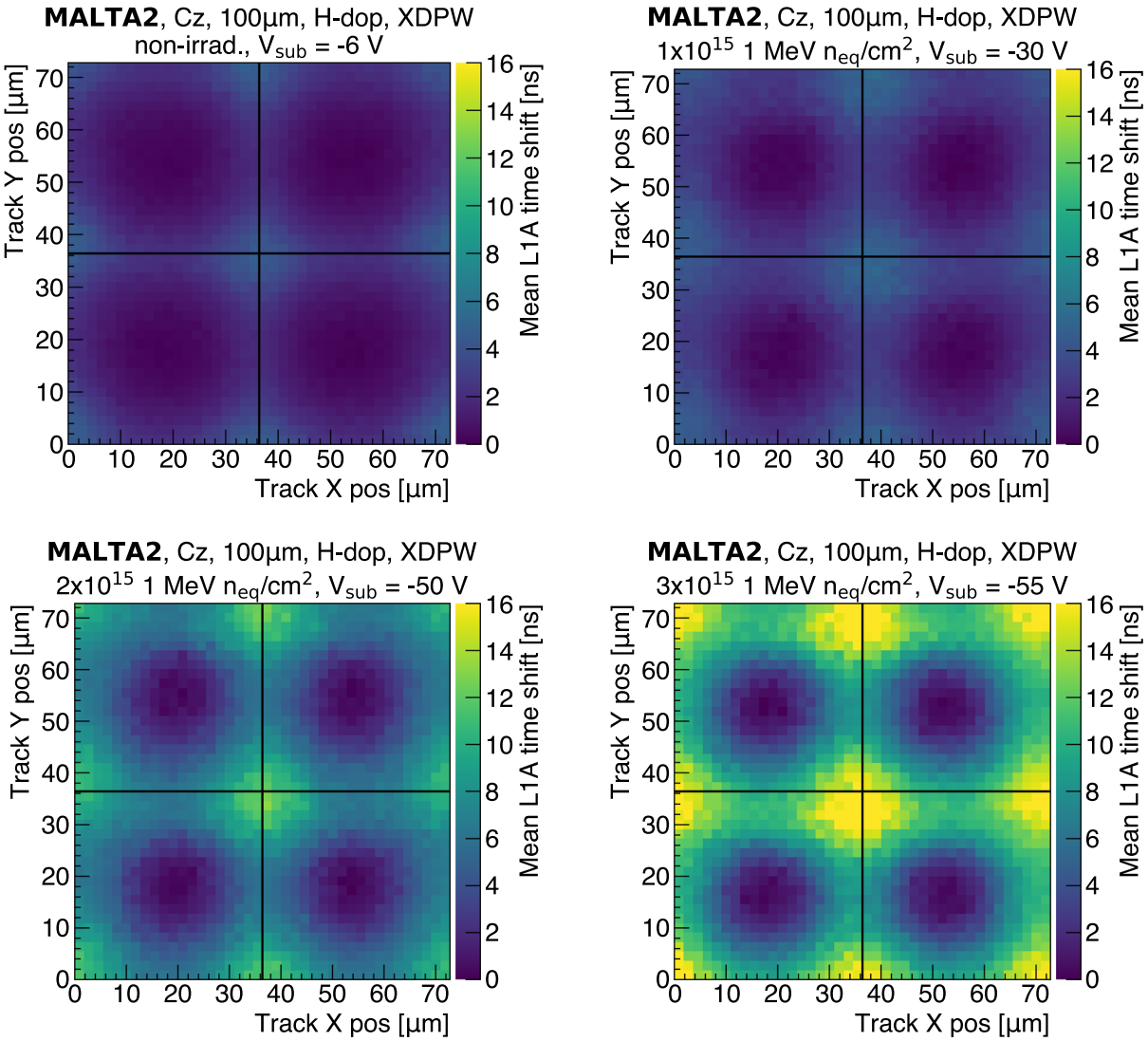

Fig. 17 Projection of the variation of the mean timing of the leading hit within a cluster with respect to a scintillator reference for four MALTA2 samples (Cz, XDPW, high doping of n^- layer, 100 µm thick, and back-side metallisation). The samples are irradiated to four different irradiation levels (non-irradiated, 1, 2, and 3×10^{15} 1 MeV n_{eq}/cm^2) and the threshold corresponds to 250, 240, 250, and 120 e^-, at $V_{sub} = -6$, -30, -50, -55V bias voltage, respectively. The leading hit time data are sorted into 1.82×1.82 µm^2 bins based on their associated track position within the pixel extracted from the telescope data. Hits from over the entire chip are projected onto a 2×2 pixel matrix. The quoted mean time value is extracted from a Gaussian fit to the core of the timing distribution for each bin relative to the bin with the smallest value. The operating conditions of the four samples correspond to the data point where the timing RMS is minimised, while the efficiency lies above 90%

ing performance is counteracted by the effect of the radiation damage, as the individual timing distributions get broader as the fluence level of the sample increases.

The results agree with the trend observed in Fig. 8, where the increase of the bias voltage results in a larger degree of charge sharing and improved charge collection from the pixel corners. For a sample irradiated to 3×10^{15} 1 MeV n_{eq}/cm^2, the very high doping of the n^- layer significantly helps to improve the RMS of the time difference distribution over a larger range of bias voltages, discussed in more detail in Sect. 5.3. Figure 15 shows the timing difference distribution of an irradiated (3×10^{15} 1 MeV n_{eq}/cm^2) MALTA2 Cz with very high doping of the n^- layer. The RMS of the distribution corresponds to 6.3 ns. When using the sliding window in-time efficiency algorithm, as used for the right image of Fig. 13, it is found that more than 95% of the cluster are collected within 25 ns and nearly 40% of the clusters are collected within a 10 ns window.

In order to better understand the impact of irradiation on the samples' timing RMS, the hit tracks are projected onto a

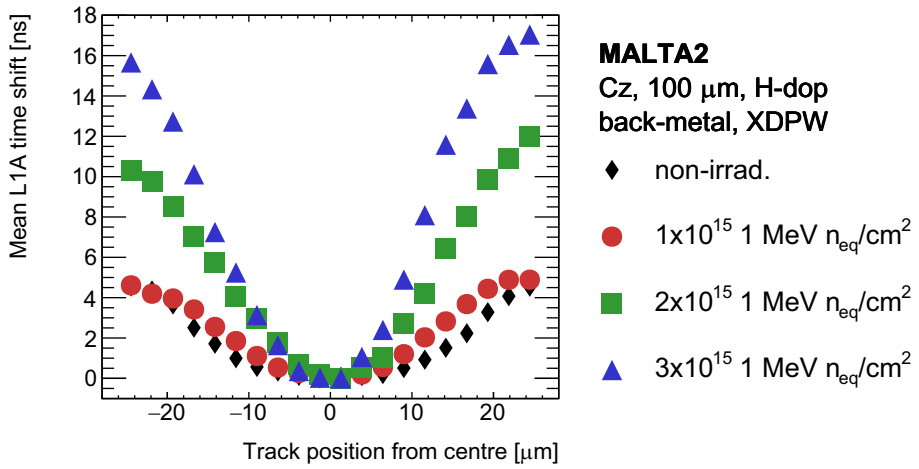

Fig. 18 Relative shift of the mean time of arrival of the leading hit within cluster with respect to the scintillator reference, as a function of the distance of the associated telescope track from the pixel centre. Results are shown for four MALTA2 samples (Cz, XDPW, high doping of n^- layer, 100 μm thick, and backside metallisation). The samples are irradiated to four different irradiation levels (non-irradiated, 1, 2, and 3×10^{15} 1 MeV n_{eq}/cm^2) and the threshold corresponds to 250, 240, 250, and 120 e^-, at $V_{sub} = -6, -30, -50, -55$V bias voltage, respectively. The operating threshold point for each sample is selected to minimise the RMS of its timing distribution. The leading hit time data are sorted into 1.82×1.82 μm^2 bins based on their associated track position within the pixel. The quoted mean corresponds to the Gaussian fit to the core of the distribution for each bin along the diagonal of the pixel

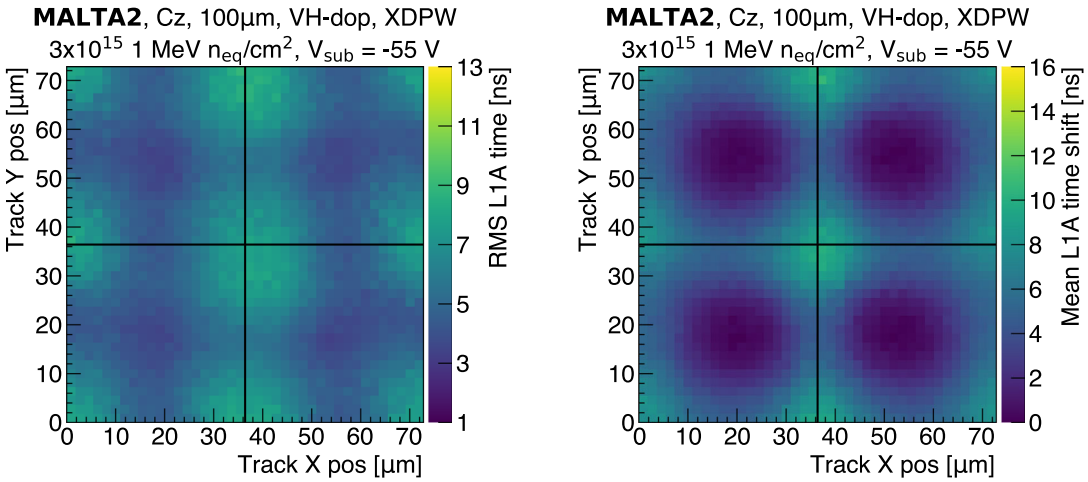

Fig. 19 The left plot shows the root-mean-squared (RMS) value of the timing of the leading hit within a cluster for each bin, while the right plot shows the projection of the variation of the mean timing of the leading hit within a cluster with respect to a scintillator reference. Both plots relate to a MALTA2 sample (Cz, XDPW, very high doping of n^- layer, 100 μm thick, and backside metallisation) irradiated to 3×10^{15} 1 MeV n_{eq}/cm^2 and operated at −55 V. The threshold corresponds to ∼ 110 e^-. The leading hit time data are sorted into 1.82×1.82 μm^2 bins based on their associated track position within the pixel. Hits from over the entire chip are projected onto a 2×2 pixel matrix. The quoted mean time value is extracted from a Gaussian fit to the core of the distribution for each bin relative to the bin with the smallest value

2×2 pixel matrix. The projection of the RMS value of the leading hit time across a pixel is shown for the four different irradiation levels (non-irradiated, 1, 2, and 3×10^{15} 1 MeV n_{eq}/cm^2) in Fig. 16. The RMS of the leading hit within a cluster varies depending on the region of the pixel being hit. The figures show that the RMS value is the smallest if the pixel is hit near the centre, whereas the value increases for corner hits, particularly at large fluences. Similarly, the mean timing of the leading hit within a cluster with respect to a scintillator reference also varies based on the region of the pixel being hit. Figure 17 shows the difference between the mean time shift of the leading hit in the cluster across the MALTA2 pixel. Comparing the individual figures for the different irradiation levels, qualitatively shows that the uniformity of the

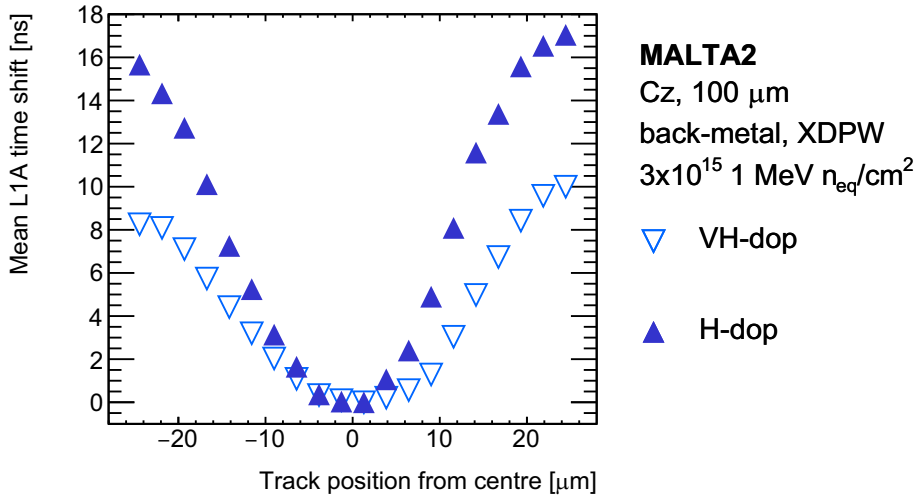

Fig. 20 Relative shift of the mean time of arrival of the leading hit within a cluster with respect to a scintillator reference, as a function of the distance of the associated telescope track from the pixel centre. Results are shown for two MALTA2 samples (Cz, XDPW, 100 μm thick, and backside metallisation) irradiated to 3×10^{15} 1 MeV n_{eq}/cm^2 and operated at $V_{sub} = -55$ V. The samples differ in the doping level of the n^- layer, i.e. high and very high, and the threshold corresponds to 120 and 110 e^-, respectively. The operating threshold point for both samples is selected to minimise the RMS of its timing distribution

mean time of arrival of the leading hit deteriorates as the fluence increases. Whereas this is not the only effect impacting the RMS value, the loss of uniformity does further increase the timing RMS values as shown in Fig. 14. To evaluate this effect in a quantitative manner, the bins along the diagonal of the MALTA2 pixel are considered for the samples shown in Fig. 17. Considering the bins along the MALTA2 pixel diagonal, Fig. 18 shows the relative shift of the mean time of hit as a function of the associated telescope track distance from the pixel centre. The quoted mean corresponds to that of a Gaussian fit to the core of the distribution for each bin along the diagonal of the pixel.

Figure 18 demonstrates that the difference between the mean time of the hit in the pixel corner and its centre is less than 5 ns in the case of a non-irradiated sample. Only a small change is observed at the fluence of 1×10^{15} 1 MeV n_{eq}/cm^2 compared to the non-irradiated case. This shift, however, grows with fluence up to more than three times the original value, reaching around 17 ns in the case of the 3×10^{15} 1 MeV n_{eq}/cm^2 sample. Further investigation has shown that the operating threshold point does not have a strong effect on the mean time shift. This observation also suggests that the variation between the samples is not due to the time walk effect. The small (∼2 ns) asymmetry between arbitrarily defined positive and negative distance of the tracks from the pixel centre may stem from the non-exact symmetry of the MALTA2 pixel. Apart from the diagonally asymmetric p-well, there are additional readout effects that can account for the absence of a perfect mirror symmetry, such as the data merging of the MALTA2 readout, mentioned in Sect. 4.3.

5.3 Effect of the doping level of the n^- layer

This method is further employed to compare the effect of the doping level of the n^- layer on the time shift at an irradiation level of 3×10^{15} 1 MeV n_{eq}/cm^2. Analogous to Figs. 17 and 16, the difference between the mean time arrival shift of the leading hit in the cluster with respect to a scintillator reference for a chip with very high doping n^- layer at 3×10^{15} 1 MeV n_{eq}/cm^2 is shown in Fig. 19 together with the RMS of the leading hit time.

The comparison of the mean time shift along the diagonal of the two samples irradiated to the fluence 3×10^{15} 1 MeV n_{eq}/cm^2 is illustrated in Fig. 20. The figure shows that out of the two MALTA2 Cz samples irradiated to the fluence of 3×10^{15} 1 MeV n_{eq}/cm^2, the sample with very high doping of the n^- layer demonstrates greater homogeneity of the mean time of hit along the pixel diagonal. As the samples otherwise share identical design parameters, this may indicate that the sample with very high doping of the n^- layer exhibits better radiation tolerance compared to the sample with high doping. Despite receiving a fluence of 3×10^{15} 1 MeV n_{eq}/cm^2, the sample with very high doping n^- layer shows comparable behaviour to a high doping n^- layer sample irradiated to 2×10^{15} 1 MeV n_{eq}/cm^2.

6 Conclusion

MALTA2 is the latest DMAPS prototype of the MALTA family. The presented combination of pixel design, process

modifications, front-end improvements and the use of high-resistivity Czochralski substrates with backside metallisation for MALTA2 have allowed to explore its performance at fluences up to 3×10^{15} 1 MeV n_{eq}/cm^2. Non-irradiated MALTA2 samples on Czochralski substrates can achieve efficiencies of 99% and an average cluster size of 2 pixels at low threshold settings (150 e^-). In these conditions, a timing resolution of σ_t=1.7 ns can be obtained, where more than 98% of the hits are collected within 25 ns. Superior performance at the highest investigated irradiation fluence (3×10^{15} 1 MeV n_{eq}/cm^2) was found on samples with very high doping of the n^- layer. Here, a maximum efficiency of 98% and an average cluster size of 1.7 pixels could be obtained at an operating threshold of 110 e^-. At these operating conditions, the RMS of the time difference distribution equals to 6.3 ns, in which 95% of the clusters are collected within 25 ns. Additionally, the irradiated MALTA2 sample with very high doping of the n^- layer exhibits a more uniform timing response across its pixel compared to a sample with high doping of the n^- layer irradiated to the same fluence. The continuous improvements of the MALTA sensor have paved the way for enhanced radiation tolerance and improved performance. As the field of high-energy physics progresses, the experiences and lessons learned from MALTA will undoubtedly contribute to the development of future detectors, pushing the boundaries of scientific frontiers even further.

Acknowledgements We are grateful to Grégory Grosset and his colleagues of Ion Beam Services in Peynier, France, for their support during the backside metallisation process. This project has received funding from the European Union's Horizon 2020 Research and Innovation programme under Grant Agreement numbers 101004761 (AIDAinnova), 675587 (STREAM), and 654168 (IJS, Ljubljana, Slovenia).

Data availability Data will be made available on reasonable request. [Authors' comment: The datasets generated during and/or analysed during the current study are available from the corresponding author on reasonable request.]

Code availability Code/software will be made available on reasonable request. [Authors' comment: The code/software generated during and/or analysed during the current study are available from the corresponding author on reasonable request.]

Funded by SCOAP[3].

References

1. ECFA Detector R&D Roadmap Process Group, The 2021 ECFA Detector Research and Development Roadmap, CERN-ESU-017 (2021)
2. M. Mager et al., ALPIDE, the monolithic active pixel sensor for the ALICE ITS upgrade. Nucl. Instrum. Methods Phys. Res. A **824**, 434–438 (2016)
3. I. Berdalovic et al., MALTA: a CMOS pixel sensor with asynchronous readout for the ATLAS High-Luminosity upgrade, in *2018 IEEE Nuclear Science Symposium and Medical Imaging Conference Proceedings (NSS/MIC)* (2018)
4. H. Pernegger et al., MALTA-Cz: a radiation hard full-size monolithic CMOS sensor with small electrodes on high-resistivity Czochralski substrate (2023). arXiv:2301.03912
5. M. Munker et al., Simulations of CMOS pixel sensors with a small collection electrode, improved for a faster charge collection and increased radiation tolerance. JINST **14**, C05013 (2019). arXiv:1903.10190
6. M. Dyndal et al., Mini-MALTA: radiation hard pixel designs for small-electrode monolithic CMOS sensors for the high luminosity LHC. JINST **15**, P02005 (2020)
7. F. Piro et al., A 1-μW radiation-hard front-end in a 0.18-μm CMOS process for the MALTA2 monolithic sensor. IEEE Trans. Nucl. Sci. **69**, 1299–309 (2022)
8. L. Flores Sanz de Acedo et al., Latest developments and characterisation results of DMAPS in TowerJazz 180nm for High Luminosity LHC. J. Phys. Conf. Ser. **2374**, P012169 (2022)
9. I. Caicedo et al., Development and testing of a radiation-hard large-electrode DMAPS design in a 150 nm CMOS process. Nucl. Instrum. Methods Phys. Res. A **1040**, P167224 (2022)
10. M. van Rijnbach et al., Radiation hardness and timing performance in MALTA monolithic pixel sensors in Tower Jazz 180 nm. JINST **17**, C04034 (2022)
11. K. Dort, Simulation Studies and Characterisation of Monolithic Silicon Pixel-Detector Prototypes for Future Collider Detectors & Unsupervised Anomaly Detection in Belle II Pixel-Detector Data (2022). https://cds.cern.ch/record/2813457
12. STAYSTIK Silver-filled Electrically Conductive Film, https://www.macdermidalpha.com/semiconductor-solutions/products/adhesives/staystik\LY1\textregistered-571
13. TAIKO Process Dicing and Polishing, https://www.dicing-grinding.com/services/dicing/
14. M. van Rijnbach et al., Performance of the MALTA telescope. Eur. Phys. J. C **83**, P581 (2023)
15. M. Kiehn et al., Proteus beam telescope reconstruction (2019). https://doi.org/10.5281/zenodo.2586736
16. K. Ambrožič et al., Computational analysis of the dose rates at JSI TRIGA reactor irradiation facilities. Appl. Radiat. Isot. **130**, 140–152 (2017)
17. L. Snoj et al., Computational analysis of irradiation facilities at the JSI TRIGA reactor. Appl. Radiat. Isot. **70**, 483–488 (2012)
18. V. Eremin et al., The origin of double peak electric field distribution in heavily irradiated silicon detectors. NIM-A **476**, 556–564 (2002)
19. ATLAS Collaboration et al., Technical design report for the ATLAS inner tracker strip detector. ATL-TDR-025, (Section 15.1) (2017)
20. L. Perktold et al., A multichannel time-to-digital converter ASIC with better than 3 ps RMS time resolution. JINST **9**, C01060 (2014)
21. G. Gustavino et al., A timing performance of radiation hard MALTA monolithic pixel sensors. JINST **18**(03), C03011 (2022)